

1 **Title:**

2 Computational study of depth completion consistent with human bi-stable perception
3 for ambiguous figures.

4
5 **Abstract**

6 We propose a computational model that is consistent with human perception of depth
7 in "ambiguous regions," in which no binocular disparity exists. Results obtained from
8 our model reveal a new characteristic of depth perception. Random dot stereograms
9 (RDS) are often used as examples because RDS provides sufficient disparity for depth
10 calculation. A simple question confronts us: "How can we estimate the depth of a no-
11 texture image region, such as one on white paper?" In such ambiguous regions,
12 mathematical solutions related to binocular disparities are not unique or indefinite. We
13 examine a mathematical description of depth completion that is consistent with human
14 perception of depth for ambiguous regions. Using computer simulation, we demonstrate
15 that resultant depth-maps qualitatively reproduce human depth perception of two kinds.
16 The resultant depth maps produced using our model depend on the initial depth in the
17 ambiguous region. Considering this dependence from psychological viewpoints, we
18 conjecture that humans perceive completed surfaces that are affected by prior-stimuli
19 corresponding to the initial condition of depth. We conducted psychological experiments
20 to verify the model prediction. An ambiguous stimulus was presented after a prior
21 stimulus removed ambiguity. The inter-stimulus interval (ISI) was inserted between the
22 prior stimulus and post-stimulus. Results show that correlation of perception between
23 the prior stimulus and post-stimulus depends on the ISI duration. Correlation is positive,
24 negative, and nearly zero in the respective cases of short (0–200 ms), medium (200–400
25 ms), and long ISI (>400 ms). Furthermore, based on our model, we propose a
26 computational model that can explain the dependence.

1 Introduction

When binocular images include no visual disparity information, as shown in uniformly colored images, how does our visual system estimate the depth or surface structure of objects? Answering this question defines the main theme of this research.

Using binocular visual information, the human visual system estimates the surface structure of objects (e.g. concave, convex, flat) in addition to those objects' positional relation. Horizontal disparity embedded within right and left retinal images provides fundamental clues that support estimation of depth differences between objects. Therefore, an important task of visual systems is to calculate the horizontal disparities (signed disparities) of matching points at every location of two retinal images. Synthetic random-dot stereograms are widely used as input stimuli for stereo vision in such experiments and theoretical studies. For a synthetic random-dot stereogram, the degree of spatial disparity is defined uniquely at every spatial location of images. However, as non-textured images and periodic textures show, general images include many spatial areas for which no unique solution of disparity can ever be determined. The white paper you might now be viewing is one example of non-unique disparity. In this case, the number of the solutions of depth is infinite because the number of possible matching points is also infinite, although our visual system must determine an appropriate solution from an infinite number of solutions of depth.

Such regions are designated herein as "ambiguous regions." Fig. 1a depicts examples of images with an ambiguous region. As Fig. 1a shows, in a solid-figure stereogram, along the left and right line segments of the rectangle or trapezoid, unique solutions of horizontal disparities are determined by finding matching points (closed line in Fig. 1b). For example, the matching point of the lower left acute angle in the left image is the obtuse angle at the left-lower point of the right trapezoid. Nevertheless, no unique disparity solution exists in the black ambiguous region at any point. Periodic textured images and the half-occlusion area should also be categorized in ambiguous regions because these areas do not provide a unique solution of disparity. The analyses described in this report specifically examine the depth completion of regions in which no disparity information is available because of uniform luminance, and not other types of ambiguity. We do not address the half-occlusion problem. Problems related to periodic texture (periodic matching point) are also beyond the scope of this article.

Completion from the disparity or depth that is determined for the non-ambiguous region (Fig. 1b) is one means of having a unique value of disparity in the ambiguous region. Computationally, "smoothness" has been used by many models as a criterion to

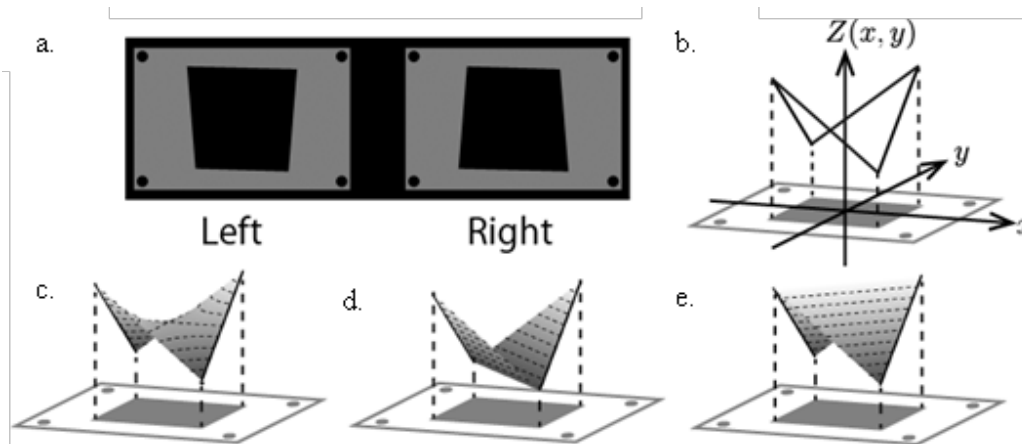


Fig. 1 a. Stereogram used for the psychological experiment explained in Section 3. Two figures show parallel view methods. **b.** Slanted lines of the depth value $Z(x,y)$ calculated using binocular disparity in a. $Z(x,y)$ is the depth at point (x,y) . **c.** Example of depth propagation using a heat conduction equation: hyperbolic paraboloid (saddle; curvature of iso-depth line $\bar{\kappa} \neq \mathbf{0}$ and curvature of flow line $\bar{\mu} \neq \mathbf{0}$). Details are presented in Section 2). **d** and **e.** Human percepts: flat depth maps. All depth contours are straight ($\bar{\kappa} = \mathbf{0}$) and parallel ($\bar{\mu} = \mathbf{0}$) lines.

1 complete depth constrained by the determined disparity (Belhumeur, 1996; Marr &
 2 Poggio, 1976; Pollard, Mayhew, & Frisby, 1985). From a psychological perspective,
 3 Würger and Landy found that humans complete depth in ambiguous regions (Würger &
 4 Landy, 1989). Georgeson et al. investigated the fundamental algorithm of human depth
 5 completion for ambiguous regions (Georgeson, Yates, & Schofield, 2009). Based on their
 6 results, they reported that humans can implement depth completion by depth
 7 propagation from the determined region of depth into ambiguous regions.

8 Some visual models use the depth propagation scheme. Fig. 1c presents one example of
 9 a depth solution determined using a propagation scheme of isotropic diffusion. The
 10 isotropic diffusion constrained with a boundary condition (depth determined from Fig.
 11 1b) generates as “smooth” a surface as possible. This “smoothness” criterion (energy
 12 function) defined by the first-order spatial derivative of the depth surface has been used
 13 for many computational models of stereopsis. For example, Nishina and Kawato (2004)
 14 propose a depth-completion model based on the heat conduction equation, which is
 15 isotropic-diffusion. In the resultant depth by isotropic-diffusion, the completed depth
 16 obligates a saddle shape. Mathematically, the saddle takes zeros of the mean curvature.
 17 Human perception differs from the “saddle” surface shown in Fig. 1c, but humans tend

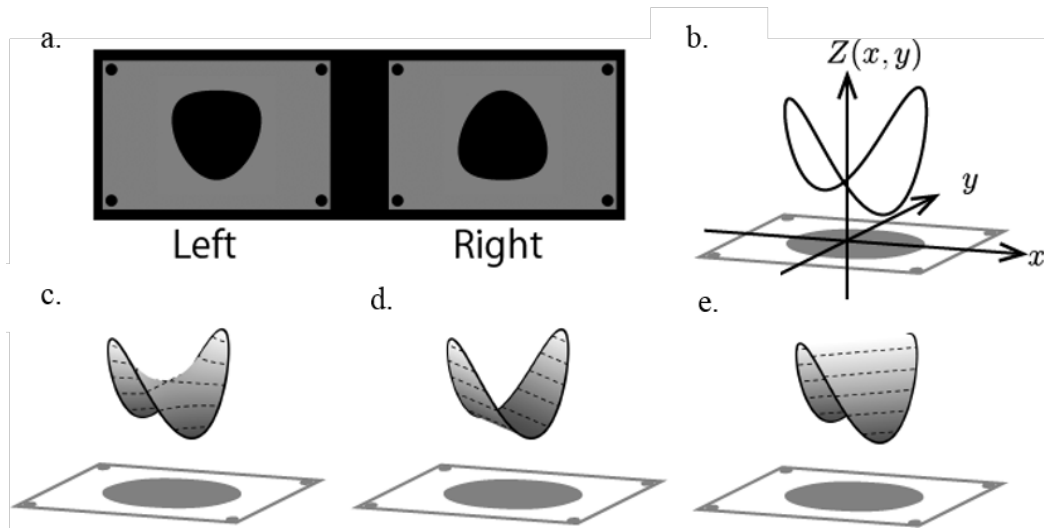


Fig. 2 **a.** Another stereo pair used in our psychological experiment. **b.** The closed curve represents the depth obtained by binocular disparity. **c.** Example of depth completion (saddle; $\bar{\kappa} \neq 0, \bar{\mu} \neq 0$) using a heat conduction equation. **d** and **e.** Surfaces perceived by humans (flat; $\bar{\kappa} = 0, \bar{\mu} = 0$). The depth contours are parallel and straight lines.

1 to recognize a “flat” surface, as depicted in Figs. 1d and 1e (Ishikawa, 2007; Ishikawa &
 2 Geiger, 2006). Similar results were found in the case presented in Fig. 2a. From
 3 observing Fig. 1d and Fig. 2d (Fig. 1e and Fig. 2e), Ishikawa and Geiger (2006) reported
 4 that perceived depth has a common mathematical property: the Gaussian curvature is
 5 zero. No neural network model has yet reproduced human perception according to Figs.
 6 1d and 1e and Figs. 2d and 2e. The present study specifically examines the development
 7 of a neural network that completes depth in the ambiguous region by spatial propagation
 8 so that the Gaussian curvature is zero.

9 This article is organized as follows. Section 2 presents our proposed model for depth
 10 completion, along with results obtained using numerical simulation with the proposed
 11 model. Section 3, with a psychological experiment, presents a new visual characteristic
 12 obtained by predictions from our model. Section 4 presents a model that is consistent
 13 with the experimentally obtained results presented in Section 3 from computational
 14 viewpoints. Section 5 includes discussion of our model from computational and
 15 physiological viewpoints. Section 6 explains our conclusions.

16
 17

2 Depth Completion by Propagation Scheme

2.1 Minimizing the First Order derivatives of surfaces

The following energy function $E_{\text{smooth}}[Z]$ presents a simple evaluation of the surface “smoothness” as quantified using the first order differentiation of a depth function $Z(x, y)$.

$$E_{\text{smooth}}[Z] = \frac{1}{2} \iint_B \|\nabla Z(x, y)\|^2 dx dy \quad (1)$$

In that equation, B represents an ambiguous region of depth. Applying the steepest descent method (or the Euler–Lagrange equation) to Eq. (1) to obtain an iterative update rule for $Z(x, y)$ that minimizes E_{smooth} , one obtains the diffusion equation shown below.

$$\frac{\partial}{\partial t} Z(x, y, t) = \left(\frac{\partial^2}{\partial x^2} + \frac{\partial^2}{\partial y^2} \right) Z(x, y, t) = \Delta Z(x, y, t) \quad (2)$$

Therein, t represents the step time during the diffusion process starting with the initial condition of $Z(x, y, 0)$. A converging $Z(x, y, t)$ is the final result of depth completion by the diffusion process. The resultant surfaces by Eq. (2) (converged Z ; $\partial Z / \partial t = 0$) are saddles which are not the expected ones presented in Figs. 1c and 2c.

2.2 Minimizing Gaussian curvature

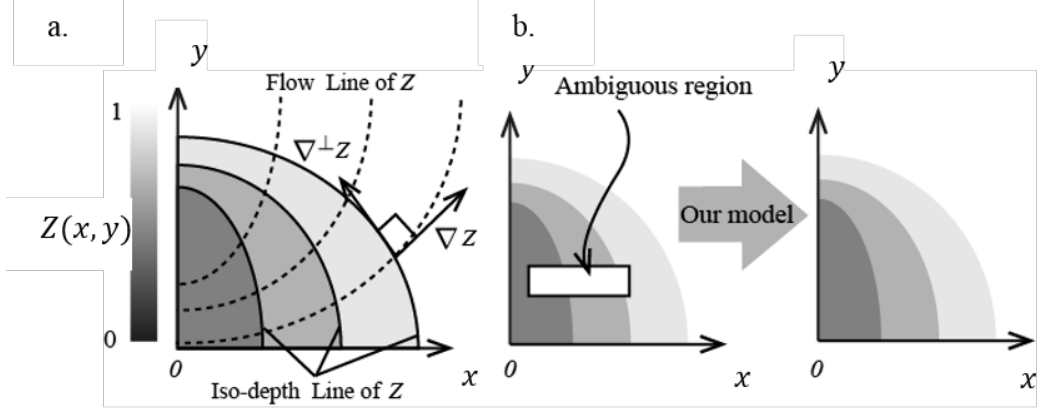


Fig. 3 Schematic explanation of curvature-related quantities. **a.** Solid curves represent iso-depth lines (contour of the depth). Dashed curves are flow lines, which are perpendicular to iso-depth lines. The gradient vector ∇Z gives the direction of the largest spatial change of $Z(x, y)$. Furthermore, $\nabla^\perp Z$ is perpendicular to ∇Z . **b.** The white rectangle of the left image is the region to be completed. Applying our model, the resultant depth map shows small curvatures of iso-depth and flow lines.

1 We discuss naïve deviation of the dynamics to obtain a “flat” surface by minimizing the
 2 Gaussian curvature. The following evaluation function $E_{\text{flat}}[Z]$ using Gaussian
 3 curvature K would be more suitable to obtain “flat” surfaces ($K(x, y) = 0$ at each point
 4 of B) reflecting human perception for the ambiguous region.

$$E_K[Z] = \frac{1}{2} \iint_B K(x, y)^2 dx dy \quad (3)$$

5 For that equation, the following definition is used.

$$K(x, y) = \frac{Z_{xx}Z_{yy} - Z_{xy}^2}{(1 + Z_x^2 + Z_y^2)^2} \quad (4)$$

6 Subscripts of Z denote partial derivatives, e.g., $Z_x \stackrel{\text{def}}{=} \partial Z / \partial x$ and $Z_{xy} \stackrel{\text{def}}{=} \partial^2 Z / \partial x \partial y$.
 7 Similarly, Z_ξ represents the directional derivative in the direction of ξ , which is
 8 perpendicular to the depth contour. Our purpose is finding the dynamics minimizing the
 9 energy function (3). Next we apply the steepest descent method to Eq. (3). Thereby, we
 10 obtain the overly complicated dynamics shown in the equation in Appendix A, which
 11 comprises 129 terms including the fourth-order derivatives of Z . Generally, accurate
 12 calculation of higher-order derivatives is difficult because of the quantized
 13 representation of images by the square lattice. Using complicated dynamics, we failed to
 14 obtain stable solutions of depth completion in our preliminary numerical experiments.
 15 Moreover, it is difficult to represent and understand the 129 terms as a neural network

1 model.

2 To overcome these difficulties, we specifically examined a substitute energy function
3 that does not compose the Gaussian curvature. The Gaussian curvature is not the only
4 option to represent the “flatness” of the depth surface.

5

6 **2.3 Minimizing Curvatures of Depth Contour**

7 Here we emphasize that we have no need to restrict ourselves to the use of the Gaussian
8 curvature to represent the surface flatness. Other curvature-related quantities
9 representing surface shapes are the mean curvature $H(x, y)$, curvature of the level-set
10 $\kappa(x, y)$, and curvature of the flow curve $\mu(x, y)$ as described below (Lindeberg, 1993). The
11 computational model proposed in this paper is based on our new theorem of the relation
12 between the condition of $\kappa^2 + \mu^2 = 0$ and $K^2 = 0$. We then derive a dynamics for depth
13 completion from a new energy function composed of κ and μ .

14 Fig. 3 presents a schematic explanation of κ and μ . Those curvatures are defined as

$$\kappa(x, y) = \frac{Z_y^2 Z_{xx} - 2Z_x Z_y Z_{xy} + Z_x^2 Z_{yy}}{(Z_x^2 + Z_y^2)^{3/2}}, \quad (5)$$

$$\mu(x, y) = \frac{(Z_x^2 - Z_y^2) Z_{xy} - Z_x Z_y (Z_{yy} - Z_{xx})}{(Z_x^2 + Z_y^2)^{3/2}}. \quad (6)$$

15 Intuitively, one can infer that κ^2 and μ^2 respectively stand for the “straightness” and
16 “parallelness” of depth contours. For example, $\kappa^2(x, y)$ being zero indicates the
17 existence of a straight line of depth contours at (x, y) ; also, $\mu^2(x, y)$ being zero means
18 that adjacent depth contours are parallel. The flatness of a surface might be evaluated
19 by zeros of $\kappa^2 + \mu^2$. Therefore, we can think of an energy function for depth completion
20 using $\kappa^2 + \mu^2$. Actually, the depth contours of Figs. 1d and 1e, and of Figs. 2d and 2e are
21 straight and parallel.

22 One might note that the numerators of Eq. (5) and Eq. (6) are sufficient to evaluate the
23 zeros of κ^2 and μ^2 . Those numerators are expressed as shown below.

$$24 \quad \bar{\kappa} = \kappa \cdot \|\nabla Z\|$$

$$25 \quad \bar{\mu} = \mu \cdot \|\nabla Z\|$$

26 We substitute $\bar{\kappa}^2 + \bar{\mu}^2 = 0$ using the curvature of the iso-depth line and flow line for
27 Gaussian curvature K for an evaluation index of flatness if we are able to prove the
28 following relation mathematically.

$$\bar{\kappa} = \bar{\mu} = 0 \implies K = 0 \quad (7)$$

29 We proved the relation above between $\{\bar{\kappa}, \bar{\mu}\}$ and K . Details are presented in Appendix
30 B. Therefore,

$$\bar{\kappa}^2 + \bar{\mu}^2 = 0 \implies K^2 = 0. \quad (8)$$

1 By spatial integration in ambiguous region B , the following relation is derived.

$$\iint_B (\bar{\kappa}^2 + \bar{\mu}^2) dx dy = 0 \Rightarrow \iint_B K^2 dx dy = 0 \quad (9)$$

2 We propose the following energy function of depth Z .

$$E_{\text{flat}}[Z] = \iint_B (\bar{\kappa}^2 + \bar{\mu}^2) \cdot \|\nabla Z\|^2 dx dy \quad (10)$$

3 An iterative method that decreases $E_{\text{flat}}[Z]$ as time progresses is also formulated by
4 application of the following steepest descend method.

$$\tau \frac{\partial}{\partial t} Z = \nabla(\Delta Z) \cdot \nabla^\perp Z + \lambda \bar{\kappa} \quad (11)$$

5 In that equation, $\nabla^\perp Z$ is perpendicular to ∇Z .

6 Depth information Z is propagated spatially by Eq. (11) because it is a kind of
7 convection–diffusion equation. The time constant is $\tau = 10$ ms and $\lambda = 0.02$ for
8 numerical simulations. Although Eq. (11) is mathematically identical to the technique
9 proposed by (Sato and Usui 2008), they did not note the relation between $\{\bar{\kappa}, \bar{\mu}\}$ and
10 K .

11

12 **2.4 Reproduction of a bi-stable solution of depth surface**

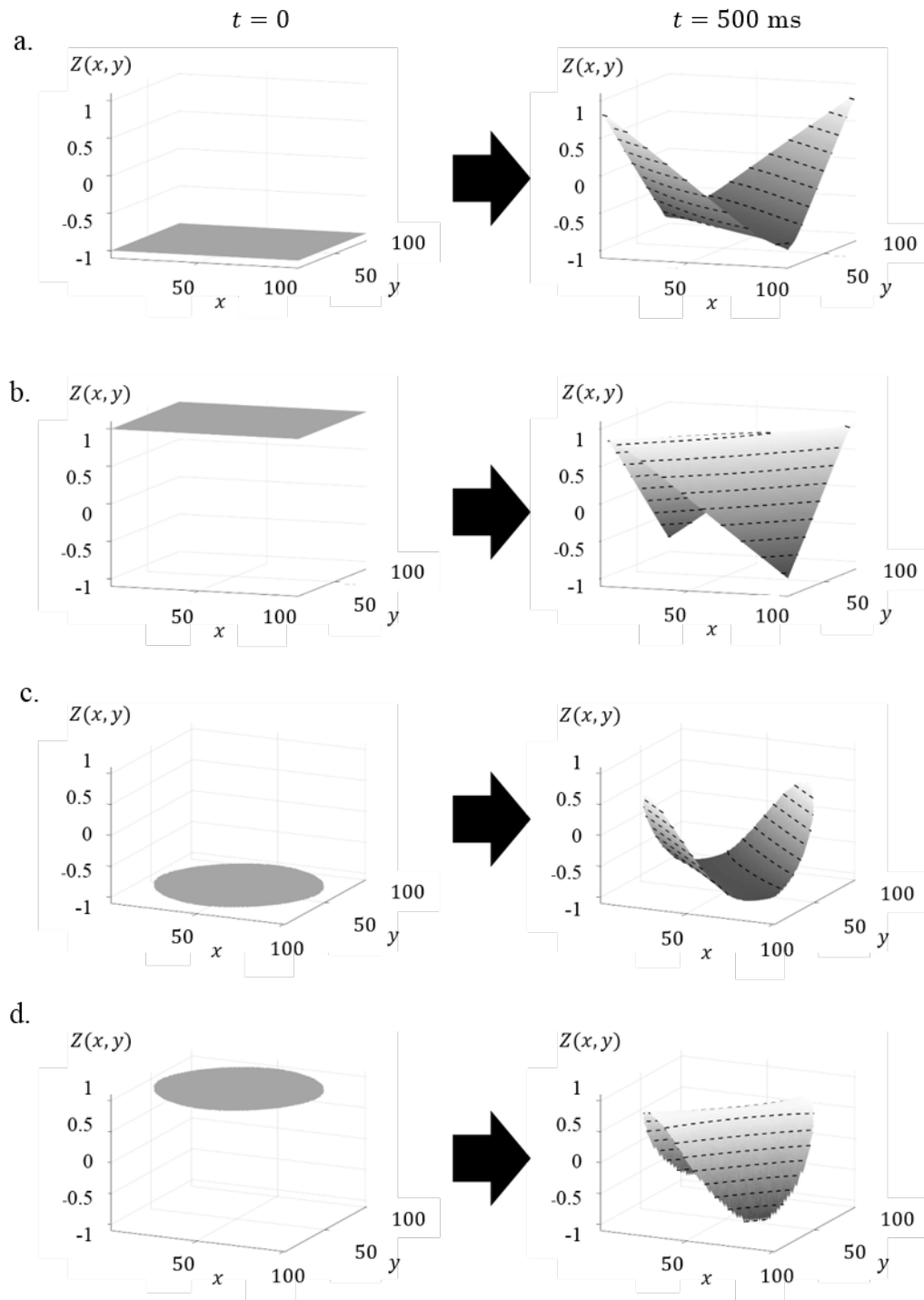


Fig. 4 Depth completion by numerical simulations starting from two initial conditions restricted with boundary conditions of two kinds, as presented in Fig. 1 and Fig. 2. The time step progresses from left to right. Boundary conditions of **a.** and **b.** (**c.** and **d.**) are the same. Depth maps converge to concave or convex flat surfaces depending on the initial conditions.

1 We next examine whether our model formulated by Eq. (11) for depth completion
2 reproduces human perception, or not. Numerical simulations of Eq. (11) were executed
3 starting from different initial values of ambiguous regions to be completed, restricted
4 with boundary conditions of two kinds. Fig. 4 presents the initial values ($t = 0$) and the
5 steady states of Z ($t = 500$ ms) by iterative updating. The depth maps converge to flat
6 surfaces. Our model presented herein also generates two solutions: A convex flat surface
7 and a concave surface. The differences of solutions are attributable to the different initial
8 values of depth in the ambiguous region. For example, Fig. 4a presents the transition
9 from the initial value of $Z(x, y, t = 0) = -1.0$ to the concave surface. Furthermore,
10 Fig. 4b presents the transition from the initial value of $Z(x, y, t = 0) = +1.0$ to the
11 convex surface. As an apparent case, a concave (convex) completed surface is obtained if
12 the initial condition is concave (convex).

13 The theoretical explanations for the strong correlation found between the shape of
14 initial surface and completed one are the energy function to be minimized and the update
15 method. The concave and convex flat surfaces give the same minimum value of the
16 energy given by Eq. (10). Therefore, the initial concave or convex flat surface is trapped
17 in one of possible wells of the energy function. In other words, when an initial value of
18 Eq. (11) is similar to that of one of those two flat surfaces, the change of initial values is
19 slight because of application of Eq. (11).

20

21 **3 Psychological Property of Depth Completion**

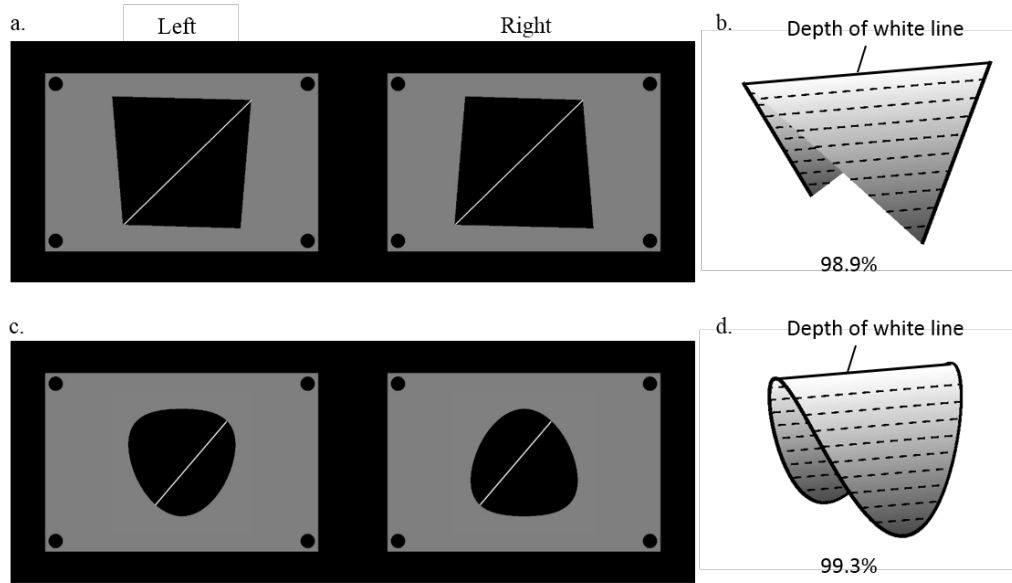


Fig. 5 Prior stimuli used in our experiment. **a.** R-boundary stimulus. Left and right panels respectively show left and right eye images. When these images are fused divergently, observers tend to perceive a convex surface as shown panel **b.** **c** and **d.** C-boundary stimulus and perceived surface from the stereo pair in panel **c.** Percentages are ratios of perception of convex surfaces (see the text for details).

1 Depth completion by our model depends on the initial condition, as presented in the
 2 previous section. Considering the initial-value-dependence of the completed surface, we
 3 conjecture that human perception within ambiguous regions is also affected by prior
 4 stimuli that correspond to the initial condition of depth. One might infer that humans
 5 would perceive a completed convex (concave) depth if they were exposed to a
 6 deterministic convex (concave) depth in advance.

7 This section presents an investigation of the plausibility of this conjecture from
 8 psychological experiments. Fig. 5a presents an example of prior stimuli presented to
 9 human subjects. Drawing slanted lines in black regions is expected to affect the depth
 10 completion in the black regions because the horizontal disparities along the lines are
 11 determined uniquely. In the case of 45 deg lines, humans would perceive a convex surface
 12 as a result of depth completion if the line captures the surface, as illustrated in Fig. 5b
 13 and Fig. 5d. By contrast, white lines slanted to 135 deg are expected to produce a concave
 14 shape of perception. Post stimuli are bi-stable surfaces similar to those of Fig. 1a and
 15 Fig. 2a. We insert the interstimulus interval (ISI) between the prior and post stimulus
 16 to assess the correlation between the shape of prior stimuli and the completed surfaces

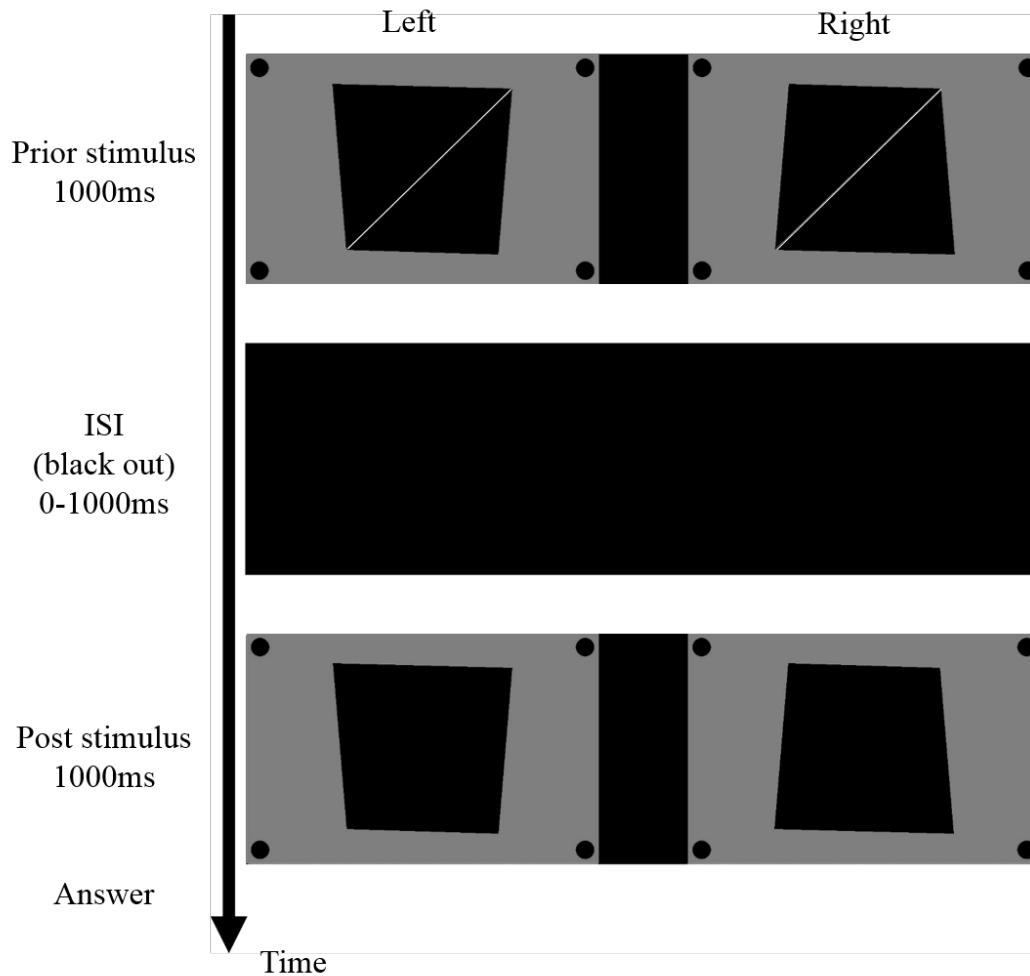


Fig. 6 Procedure of our experiments. A prior stimulus is presented for 1000 ms. After disappearance of the prior stimulus, the display is blacked out for 0–1000 ms randomly (ISI). A bi-stable stimulus (post stimulus) is presented for 1000 ms after the ISI phase.

1 of post stimulus. Humans will perceive a convex (concave) surface if the prior stimulus
 2 is convex (concave) if an ISI is short. Consequently, we would observe a positive
 3 correlation between the surface shape of post and prior stimuli. Longer ISI is expected
 4 to show no correlation between stimuli because of attenuation of the effects of prior
 5 stimuli.

6 **3.1 Method**

7 3.1.1 Setup

8 **Fig. 6** presents a schematic explanation of our psychophysical experiments. We
 9 designed our software for use with psychophysical experiments using MATLAB extended

1 with the Psychophysics Toolbox (Brainard, 1997; Kleiner & Brainard, 2007; Pelli, 1997).
2 Visual stimuli were presented on a color display (XL2410T; BenQ Corp.) via a graphics
3 card (GeForce GTX560; NVIDIA Corp.). The display refresh rate was 60 Hz for each eye
4 with 1920×1080 pixels of resolution. Human participants wore liquid crystal shutter
5 goggles (3D vision 2; NVIDIA Corp.) for stereo perception. Stereo stimuli were presented
6 at the viewing distance of 1.5 m. Participants sat on a chair with a chin rest. After ISI, a
7 post stimulus appeared. Then participants were asked to press a button on a keyboard
8 according to their perception of the post stimulus, after selection from three candidates
9 (concave, saddle, and convex surface; 3AFC).

10 Nine participants (23–35 years) were examined in our experiments. All were naïve to
11 the purpose of these experiments. All had normal or corrected-to-normal vision. This
12 experiment, which was approved by the ethics committee of the University of Electro-
13 Communications, was conducted in accordance with approved guidelines. All
14 participants gave informed consent before participation.

16 3.1.2 Stimuli

17 We prepared boundary conditions of depths of two kinds. One is rectangular. Another
18 is a circular boundary condition, as shown Fig. 5. We designate them respectively as R-
19 boundary and C-boundary conditions and stimuli.

20 Prior stimuli were stereograms with white slanted lines by which mono-stable
21 perception is expected to be obtained as depicted in black ambiguous regions (Fig. 5). We
22 first examine if the white lines in Figs. 5a and 5c captured surfaces to ascertain whether
23 these lines cause convex (not concave) perceptions, as shown in Figs. 5b and 5d. The
24 luminances of black and white regions were, respectively, 0.23 cd/m^2 and 171 cd/m^2 . The
25 luminance of the grey background was 34.9 cd/m^2 . To support binocular fusion, four solid
26 circles surrounded the stimulus. We collected 180 and 135 responses from the nine
27 participants for the R-boundary condition (Fig. 5a) and C-boundary condition (Fig. 5c),
28 respectively. Percentages in Fig. 5 are the answer ratios of convex surface perception.
29 When Fig. 5a was viewed, eight participants always perceived a convex surface, although
30 one participant occasionally perceived a concave surface twice with two popping up
31 corners connected with the white line (the white line did not capture the surface, but
32 separated from the surface). For the stimulus of Fig. 5c, perception of line-separated-
33 from-surface occurred only once. Similar results were obtained for the case of white lines
34 slanted 135 degrees. We regarded the line-separated-from-surface perception as
35 uncommon and inferred that the slanted lines certainly capture the surfaces as shown
36 in Figs. 5b and 5d.

1 In the main experiment, a prior stimulus was presented for 1000 ms. Then the post
 2 stimulus was presented for 1000 ms after randomized duration of ISI (Fig. 6). We
 3 prepared eight conditions of stimuli: 2 (R-boundary and C-boundary conditions of
 4 stimuli) \times 2 (orientation of slanted lines) \times 2 (swapped left and right images). Stimuli of
 5 those conditions were presented in random order. Durations of ISIs were determined
 6 using the stochastically uniform distribution of 0–1000 ms.

7 One session comprised $25 \times 8 = 200$ trials with random ISIs for the eight stimulus
 8 conditions. Each participant joined one session. Two of nine participants joined in an
 9 additional 400 trials.

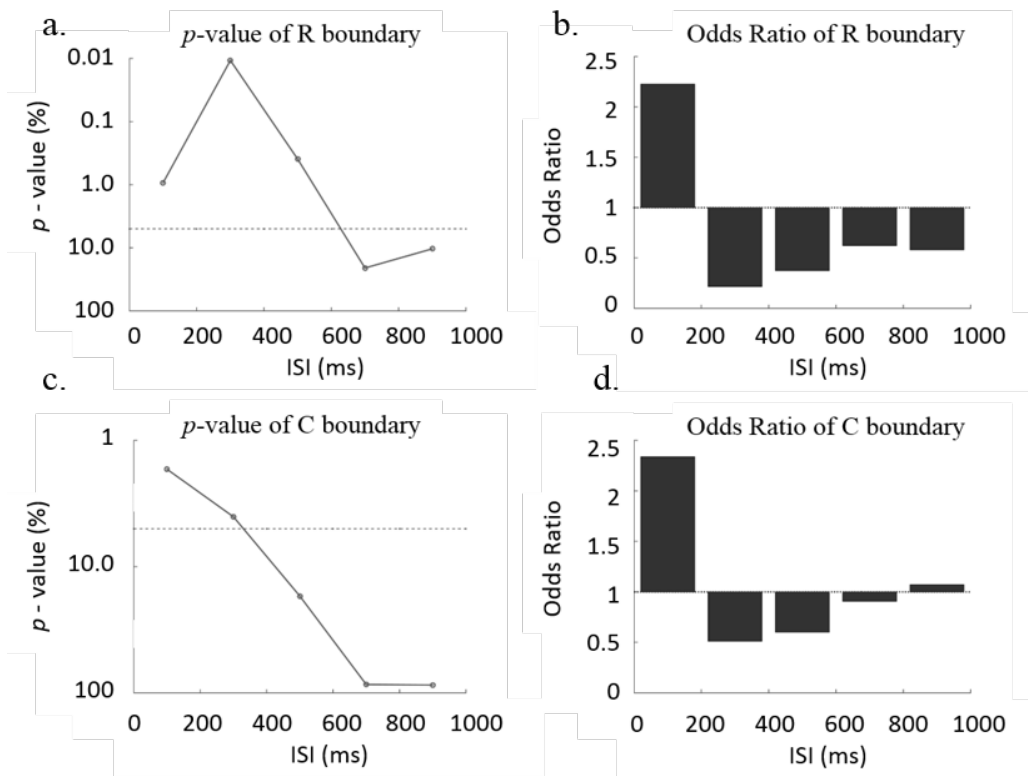


Fig. 7 Statistical analysis of psychological experiments. **a.** p -value of each ISI bin. The dotted line shows the 5% significance level. p -values above the dotted line show $p < 0.05$. **b.** Odds ratio of each bin for R-boundary stimuli. $OR > 1$ signifies a positive correlation between a prior and post stimulus. $OR = 0$ means a negative correlation. The dotted line is $OR = 1$, which signifies no correlation. For C-boundary stimuli, panels c and d respectively show the p -value and OR.

3.2 Results

We applied Fisher’s exact test against the following null hypothesis: the shapes of the prior stimuli and the post stimuli are independent. All responses from all participants are binned in 200 ms bins of ISI. Significant dependence was found between prior and post stimuli when $0 \leq \text{ISI} < 600$ ms for the R-boundary condition, and when $0 \leq \text{ISI} < 400$ ms for the C-boundary condition ($p < 0.05$; Figs. 7a and 7c).

To ascertain whether the correlation is positive or negative in the bins of $0 < \text{ISI} \leq 200$ and $200 \leq \text{ISI} < 400$, we evaluated the odds ratio of data of each bin (Figs. 7b and 7d). An odds ratio ($\text{OR} \geq 0$) is calculated from a 2×2 contingency table. In our case, the 2×2 tables were obtained by excluding the responses of “saddle.” The case of $\text{OR} = 1$ signifies no correlation. $\text{OR} > 1$ indicates a positive correlation between prior and post stimuli. Given such a result, human participants tend to perceive a convex (concave) surface in an ambiguous region if the prior is also convex (concave). Alternatively, $\text{OR} = 0$ represents a negative correlation; the shape of completed surface is opposite to the prior stimulus.

For $0 < \text{ISI} \leq 200$ ms, we found positive correlation, as we had expected. This phenomenon is apparently trivial because it is easily explained by our model, in which the steepest descent method is adopted. An initial value corresponding to a prior stimulus will be trapped by an energy well near the state of the initial value.

An unforeseen and noteworthy negative correlation was found when $200 \leq \text{ISI} < 400$ ms. As a summary of the psychological experiments, we showed that a positive aftereffect appears if ISI is short ($0 \leq \text{ISI} \leq 200$), although middle ISIs ($200 \leq \text{ISI} < 400$) cause negative aftereffects on surface completion in ambiguous regions. No significant evidence or trend was found in the case of longer ISI conditions ($600 \leq \text{ISI} < 1000$ ms).

The results described above rely on an assumption that the white slanted line induces unique perception, but that is not always true (see the percentages of Fig. 5). Future works shall include an investigation of the on-time evaluation of human perception for the prior stimuli during experiments.

1 4 **Model of ISI-dependent perception**

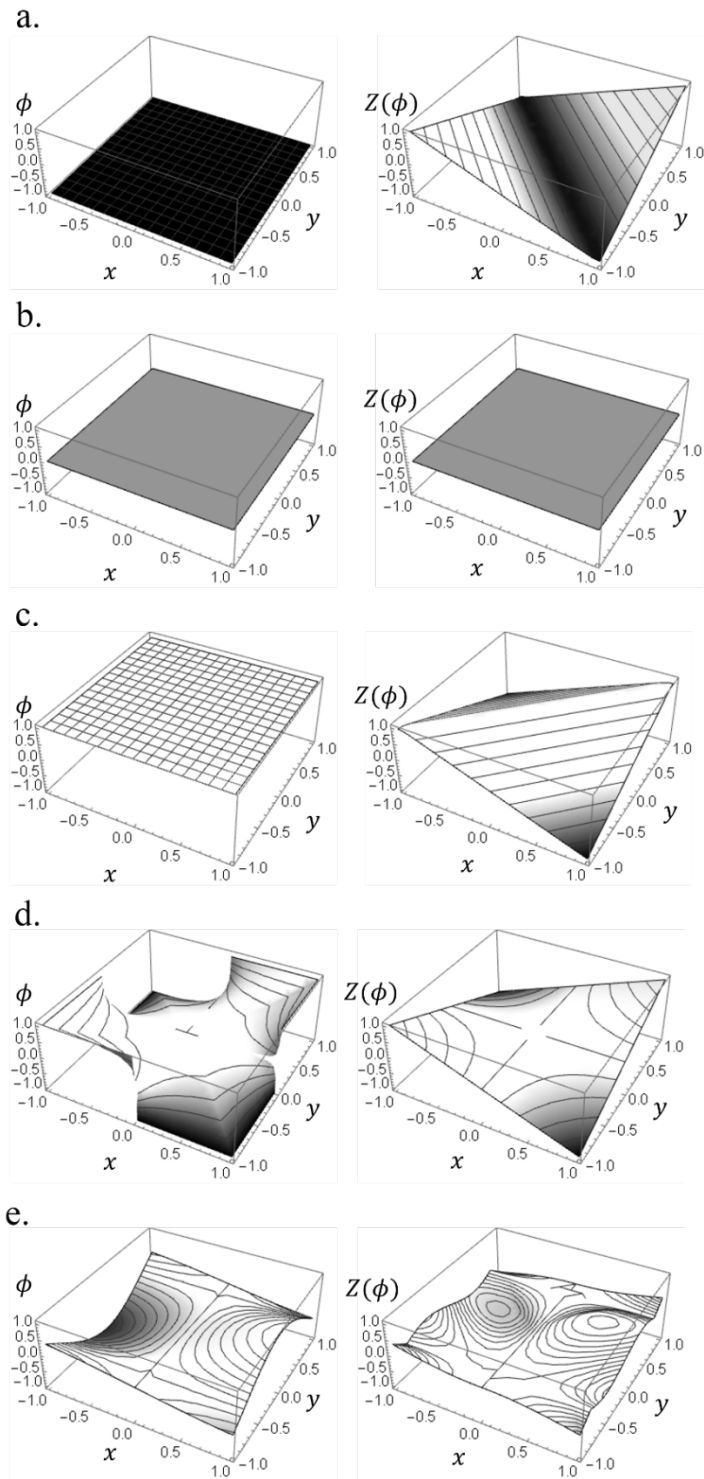


Fig. 8 a, b, c. Examples of depth maps $Z(\phi(x, y))$ represented using a scalar parameter $\phi(x, y)$. A concave, a flat depth of zero, a convex, and their intermediate depth maps are represented by the single scalar parameter ϕ . d, e. The saddle surface and complex surface can be represented using $\phi(x, y)$.

1 The model formulated by Eq.(11) in Section 2 successfully completes the “flat” surface
 2 of depth, but it does not account for the negative correlation between the perceived depth
 3 of the prior and post stimuli for $ISI > 200$ ms. When a prior stimulus, which is the initial
 4 condition $Z(x, y, t = 0)$ of Eq. (11), is convex (concave), the resultant completed depth is
 5 also convex (concave) for any ISI. To reproduce the ISI-depending completion of depth,
 6 we develop an alternative model in this section.

7 Although we considered improving the dynamics of Eq.(11) that obtain an opposite
 8 surface by adding acceleration term, no expected results were obtained. Then, for simple
 9 modeling, we limited the solution space of $Z(x, y)$ and derived a new dynamics based on
 10 Eqs (10) and (11) as follows. Specifically, we represent depth maps $Z(x, y)$ by a single
 11 scalar parameter $\phi(x, y)$ so that $Z(\phi(x, y))$ denotes a concave surface ($\phi = -1$), flat
 12 ($\phi = 0$), and a convex surface ($\phi = +1$), as shown in Fig. 8. The following equation
 13 formulates the parametric $Z(\phi(x, y))$.

$$Z(\phi(x, y)) = \begin{cases} \phi(x, y) \cdot Z_{\wedge}(x, y), & \text{if } \phi > 0 \\ 0, & \text{if } \phi = 0 \\ -\phi(x, y) \cdot Z_{\vee}(x, y), & \text{otherwise.} \end{cases} \quad (12)$$

14 Therein, the functions $Z_{\vee}(x, y)$ and $Z_{\wedge}(x, y)$ respectively produce a concave and a
 15 convex depth map.

16 As shown in Fig. 8, $\phi(x, y) = -1, 1$ respectively represent $Z_{\vee}(x, y)$, $Z_{\wedge}(x, y)$. We can
 17 present not only concave and convex surfaces, but also a saddle surface and surfaces
 18 other than $Z_{\vee}(x, y)$ and $Z_{\wedge}(x, y)$ by setting different values of $\phi(x, y)$ at each point
 19 (x, y) , as shown in Figs. 8d and 8e. Noting that $Z(\phi(x, y))$ is a composite function of
 20 $\phi(x, y)$, the left side of Eq. (11) can be rewritten as shown below.

$$\frac{\partial Z}{\partial t} = \frac{\partial Z}{\partial \phi} \cdot \frac{\partial \phi}{\partial t} \quad (13)$$

21 Because of Eq.(12), we can obtain the following expression.

$$\tau \frac{\partial Z(\phi)}{\partial \phi} = \begin{cases} Z_{\wedge}, & \text{if } \phi > 0 \\ 0, & \text{if } \phi = 0 \\ -Z_{\vee}, & \text{otherwise.} \end{cases} \quad (14)$$

22 Therefore, to obtain a new model for depth completion, the dynamics $\partial \phi / \partial t$ plays a key
 23 role in reproducing the experimentally obtained results in Section 3. $\partial \phi / \partial t$ represents
 24 state-transition of depth map during ISI. Hereinafter, we consider the transition of depth
 25 maps during ISI.

26 First, we describe the energy function using ϕ to evaluate flatness. Figs. 8a and 8c of
 27 stable states respectively show $\phi(x, y) = -1$ (concave surface) and $\phi(x, y) = +1$
 28 (convex surface). The constant flat depth $Z(x, y) = 0$, which could be a completed depth

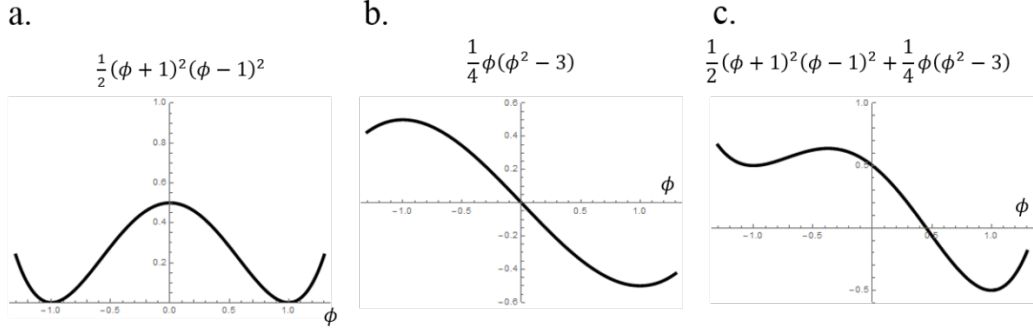


Fig. 9

The landscape of the energy function at each point (x, y) . For simple presentation, (x, y) is omitted for $\phi(x, y)$. a. The double-well potential function represents two possible perceptions. The effect of the energy increase by adaptation to a pattern corresponding to the left well can be represented by the function **b**. An example of the total energy **c**, has two wells. The energy of the left well is greater than that of the right well.

- 1 for long $ISI > 1000$ ms, is obtained by setting $\phi(x, y) = 0$. Those representative “flat”
 2 depths are $\phi(x, y) = \text{const}$. Therefore, we define the energy function to evaluate flatness
 3 as (Fig. 9a):

$$E_1[\phi] \stackrel{\text{def}}{=} \frac{1}{2} \iint_B \|\nabla \phi(x, y)\|^2 dx dy, \quad (15)$$

- 4 because the following relation holds (Appendix C).

$$E_1[\phi] = 0 \implies E_{\text{flat}}[Z] = 0$$

- 5 Second, we formulate energy function $E_2[\phi]$ as follows, so that the value is the
 6 minimum for $\phi = +1$ or -1 .

$$E_2[\phi] \stackrel{\text{def}}{=} \frac{1}{2} \iint_B (\phi(x, y) + 1)^2 (\phi(x, y) - 1)^2 dx dy \quad (16)$$

- 7 A flat concave or convex surface will be obtained by minimizing $E_1[\phi] + E_2[\phi]$.

- 8 Finally, to reproduce alternation of surface from a concave (convex) to a convex
 9 (concave) surface, we formulate the effect of prior stimulus as shown below.

$$E_3[\phi] \stackrel{\text{def}}{=} \iint_B \frac{1}{4} \phi(x, y) (\phi^2(x, y) - 3) dx dy \quad (17)$$

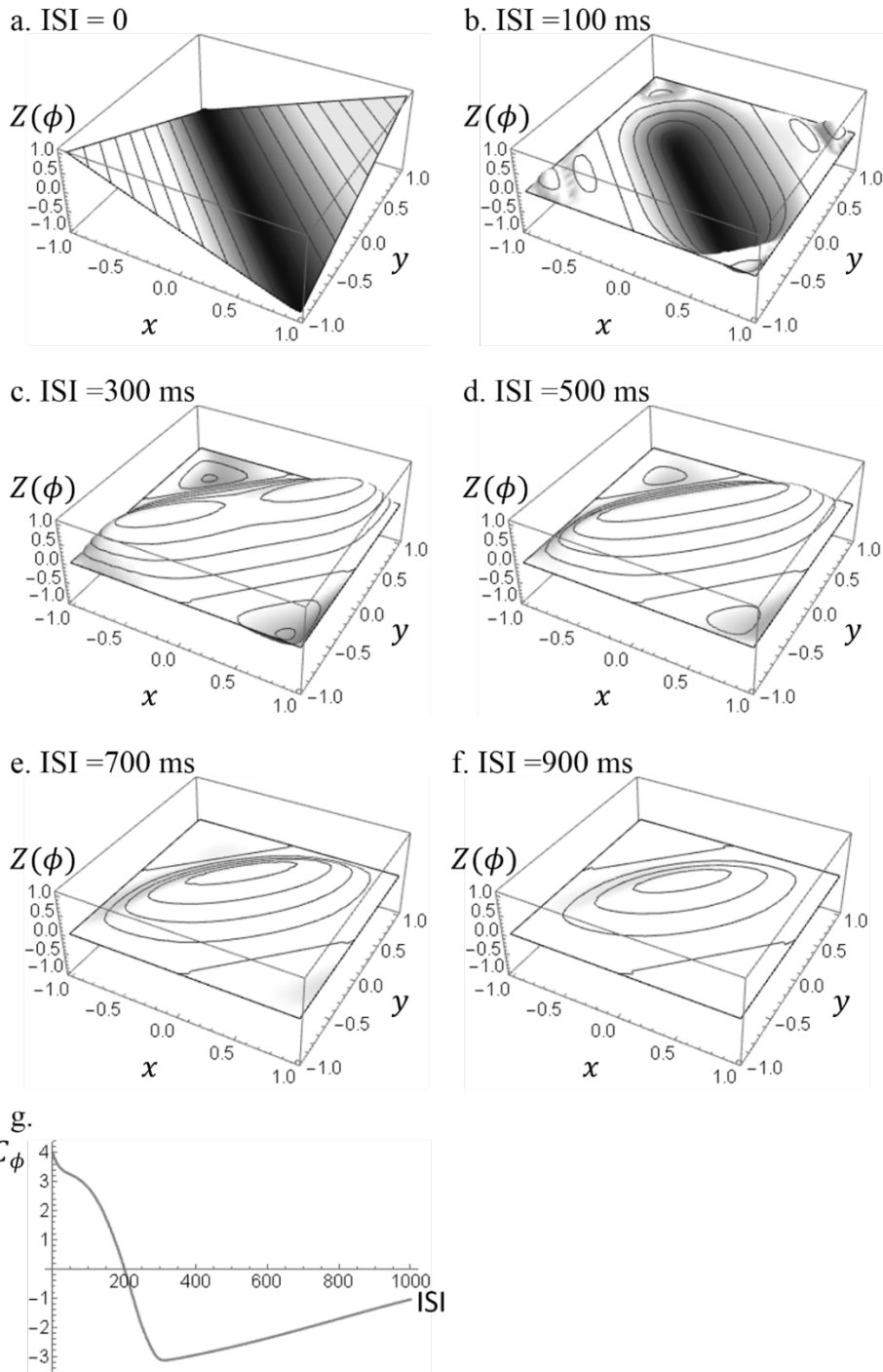


Fig. 10 Panels **a**, **b**, **c**, **d**, **e**, and **f** respectively show depth maps at the finishing times of $ISI=0$, 100, 300, 500, 700, and 900 ms. These maps are used as initial values of depth completion for ambiguous regions after ISI. Boundary conditions are $\mathbf{Z} = \mathbf{0}$ equivalent with $\phi = \mathbf{0}$. **g.** Horizontal and vertical axes respectively show ISI and $C_\phi(t)$. $C_\phi(t)$ is plotted every 5 ms of ISI.

1 The equation for $E_3[\phi]$ above represents the elevation of potential for the concave
 2 surface of prior stimuli. It is noteworthy that $E_3[\phi]$ takes its local maximum at $\phi = -1$,
 3 which is the case of the concave surface of prior stimuli (see Fig. 9b). By contrast, $-E_3[\phi]$
 4 represents the case of convex surface of prior stimuli.

5 Consequently, the total energy function over space B is formulated as shown below as

$$F[\phi] = \beta_1 E_1[\phi] + \beta_2 E_2[\phi] + \beta_3 E_3[\phi] , \quad (18)$$

6 where β_1 , β_2 , and β_3 are positive scalars. These parameters signify the strength of the
 7 visual effect by prior stimuli. In the case of a convex surface being prior stimuli, the third
 8 term of the equation for $+E_3$ above is replaced with $-E_3$. Thereby, we introduce the
 9 effect of adaptation into the proposed model.

10 We introduce time variable t for ϕ to decrease the $F[\phi]$ by application of the
 11 steepest decent method. Thereby, we obtain

$$\tau \frac{\partial \phi}{\partial t} = \beta_1 \cdot \Delta \phi + \beta_2 \cdot 2\phi(1 - \phi^2) + \beta_3 \cdot \frac{3}{4}(1 - \phi^2), \quad (19)$$

12 We perform numerical simulations of Eq. (13) substituting Eq.(14) and Eq.(19) in the
 13 case of presenting the R-concave surface as a prior stimulus signified by $\phi(x, y, t = 0) =$
 14 -1 . Because no depth information is available at the ISI period, β_2 and β_3 are
 15 decreasing functions with respect to ISI duration t . We set the following.

$$\beta_2(t) = \beta_3(t) = e^{-\frac{t}{20}}$$

16 Other parameters are $\tau = 10$, $\beta_1 = 0.0001$. Time $t = 0$ represents the start of ISI.
 17 Region B is a rectangular region of $|x| < 1$ and $|y| < 1$. The boundary condition
 18 $Z(x, y) = 0$ is equivalent to $\phi(x, y) = 0$.

19 Fig. 10 shows Z at $t = 0, 100, 300, 500, 700$, and 900 ms. Equation (13) was applied in
 20 the inner rectangular region. Results show that the state of Z at $t = 0$ ms (ISI=
 21 0 ms) is similar to the concave initial state. Depth completion by Eq. (11) starting with
 22 the initial value of Fig. 10b converged to a concave depth surface. This result implies
 23 positive correlation between the prior stimulus and post stimulus for short ISI.
 24

25 Results show that the state at $t = 300$ ms is now convex (Fig. 10c), which is the
 26 opposite state to the prior stimulus (concave). The change of state from $\phi = -1$ to $\phi =$
 27 $+1$ occurred, although an energy barrier exists between them, as shown in Fig. 9c.

28 Consequently, the positive/negative correlation dependent on the duration of ISI is
 29 explainable by an adaptation effect by prior stimuli. Longer ISI attenuates the effect of
 30 adaptation by prior stimuli, giving results of no correlation between prior and post
 31 stimuli because the state of Z converges to $\phi = 0$, meaning that $Z = 0$ (Fig. 8b).
 32 Quantitatively equivalent results were obtained for the C-boundary condition.

33 Subsequently, we compare odds ratio in Section 3 with the alternative model above by

1 calculating correlation between prior and post stimuli as follows.

$$C_\phi(t) = \iint_{\mathbf{B}} \phi_{\text{prior}}(x, y) \cdot \phi(x, y, t) dx dy \quad (20)$$

2 Therein, $\phi_{\text{prior}}(x, y)$ represents ϕ ($= +1$ or -1) of prior stimulus and $\phi(x, y, t)$ given
3 by Eq.(19) represents an internal state of completed depth at each time of ISI. For
4 example, in the case of $\text{ISI} = 0$ ms, $\phi(x, y, t = 0)$ of Fig. 10a is identical to Fig. 8a.

5 We assume that prior stimulus is a concave surface, that is $\phi_{\text{prior}}(x, y) = -1$. We
6 calculated $C_\phi(t)$ every 5 ms for $\text{ISI}=0\text{--}1000$ ms. This result is presented in Fig. 10g. The
7 result in Fig. 10g is qualitatively similar to the odds ratio in Fig. 7b.

8 The odds ratio includes stochastic elements. By contrast, our model proposed in this
9 paper is deterministic. Therefore, we must incorporate a stochastic perception of humans
10 into the proposed model.

11

5 Discussion

5.1 Physiological evidence for the proposed model

We discuss whether our model is implementable as a neural network from the viewpoint of existing physiological evidence. We introduce a local coordinate system (η, ξ) as shown in Fig. 11a. Then, Eq. (11) is rewritten as shown below.

$$\tau \frac{\partial}{\partial t} Z = (\nabla \Delta Z) \cdot \nabla^\perp Z + \lambda \bar{\kappa} = Z_\xi \left(\frac{\partial}{\partial \eta} Z_{\eta\eta} + \frac{\partial}{\partial \xi} Z_{\xi\eta} \right) + \lambda Z_{\eta\eta}$$

Therefore,

$$\tau \frac{\partial}{\partial t} Z = Z_\xi \frac{\partial}{\partial \eta} \Delta Z - \Delta Z + (\Delta Z + \lambda Z_{\eta\eta})$$

Let the surface $Z(x, y)$ be represented approximately as a quadric surface, then $\partial \Delta Z / \partial \eta = 0$. Consequently, Eq. (11) can be described as

$$\tau \frac{\partial}{\partial t} Z \simeq -\Delta Z + (\Delta Z + \lambda Z_{\eta\eta}) \quad (21)$$

The dynamics up to the first term are implementable as a neural network using average of input from a four-neighbor neuron as an amount of change, as shown in Fig. 11b.

Regarding the second term, the amount at origin point and Shape Index (Koenderink, 1990) are proportional (see Fig. 11d). Katsuyama and his colleagues found that neurons in CIP respond selectively to Shape Index (Katsuyama, Naganuma, Sakata, & Taira, 2006). Then, the possibility exists that the second term of Eq. (21) is encoded in CIP.

Subsequently, we discuss the neural network diagram of the model in Section 4. For simple discussion, we describe the case without the effect of prior stimuli: $E_3[\phi] = 0$. In this case, because of $E_3[\phi] = 0$,

$$F[\phi] = \beta_1 E_1[\phi] + \beta_2 E_2[\phi].$$

To simplify our discussion, let $\beta_1 = \beta_2 = 1$, then the dynamics Eq.(19) is

$$\tau \frac{\partial \phi(x, y)}{\partial t} = \Delta \phi - 2\phi(\phi^2 - 1).$$

We show a neural network diagram representing the dynamics explained above in Fig. 11c. The dynamics up to the first term is implementable as a neural network using the average of input from a four-neighbor neuron as an amount of change, as shown in Fig. 11c.

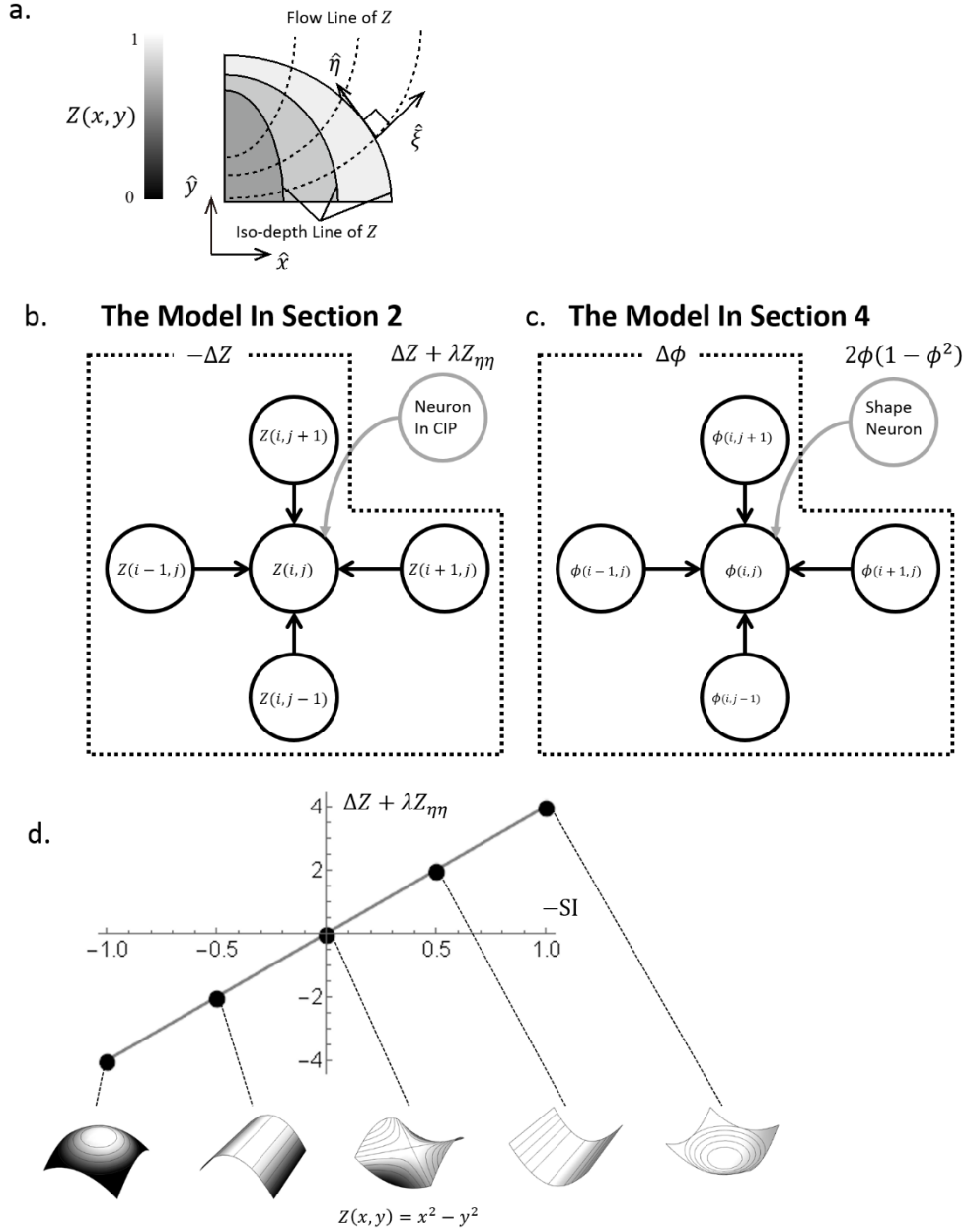


Fig. 11 **a.** Local coordinate system (ξ, η) is defined at each spatial position of (x, y) . Direction $\hat{\xi}$ is parallel with ∇Z ; $\hat{\eta}$ is perpendicular to $\hat{\xi}$. **b.** Neural network diagram of the model in Section 2. Circles present neurons. $Z(i, j)$ represents depth at spatial position (i, j) . $-\Delta Z$ at (i, j) is calculable using 4-neighbors of neuron. $Z(i, j)$ is updated iteratively using output from 4-neighbors and neurons in CIP. **c.** Neural network diagram of the model in Section 4. **d.** Relation between our model and the Shape Index (SI) for each shape. The vertical axis represents the value of the second term in Eq. (21) at the origin point. The horizontal axis represents $-\mathbf{SI}$.

1 Regarding the second term, when a surface is concave (Fig. 8a), flat (Fig. 8b), or convex
 2 (Fig. 8c), the amount is equal to zero at any point. However, when a surface is a saddle
 3 (Fig. 8d), the amount is not equal to zero. Katsuyama and his colleagues reported that
 4 neurons in CIP respond selectively to the saddle shape (Katsuyama, Naganuma, Sakata,
 5 & Taira, 2006). Then, it is possible that the second term represents a signal from a saddle
 6 selective neuron. Consequently, the proposed models of the present study are
 7 implementable as a neural network.

9 **5.2 Comparison between a Second-Order differential Model** 10 **and Isotropic-diffusion for one-dimensional surface completion**

11 To provide information about the generality of proposed model, we compare results
 12 between a second-order differential model and isotropic diffusion for simpler one-
 13 dimensional surface completion. In the case of isotropic diffusion, Nishina & Kawato
 14 (2004) proposed a depth completion model based on the heat conduction equation for one
 15 dimension.

16 To apply our model for one-dimensional surface completion, because curvature
 17 information is described with spatial second order differential, we define the energy
 18 function as follows.

$$E_{\text{flat-1}}[Z] = \int_B \left(\frac{d^2}{dx^2} Z(x) \right)^2 dx. \quad (22)$$

19 Applying the steepest descent method to Eq. (22) to obtain an iterative update rule for
 20 $Z(x)$ that minimizes $E_{\text{flat-1}}[Z]$, one obtains the diffusion equation shown below.

$$\frac{\partial}{\partial t} Z(t, x) = - \frac{\partial^4}{\partial x^4} Z(t, x). \quad (23)$$

21 Fig. 12 presents results of numerical simulation using Eq. (23) and isotropic diffusion.

22 Isotropic diffusion completes the flat surface, but continuity is not maintained around
 23 the boundary. However, Eq. (23) completes the smooth surface but continuity is
 24 maintained around the boundary. Spline interpolation yields similar results to those of
 25 Eq. (23).

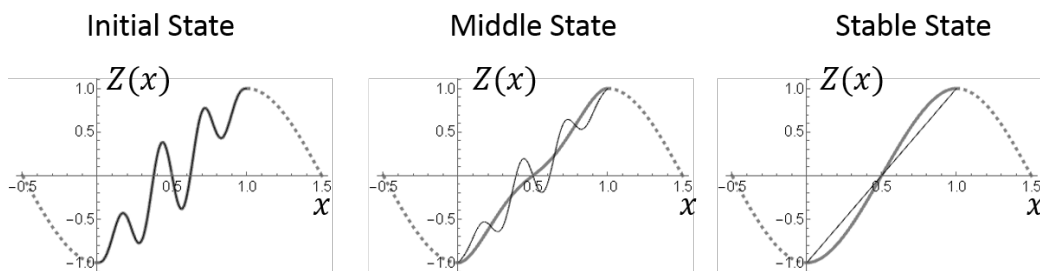


Fig. 12 Comparison for the one-dimensional case between isotropic diffusion and the fourth derivative model. Black thin line: Isotropic diffusion. Grey bold line: Diffusion based on the second order differential. Dotted line: Boundary Condition. Left: Initial state. Center: Middle state. Right: Stable State.

6 Conclusions

Our proposed computational model for depth completion is consistent with human perception: it completes the depth values as a “flat” surface quantified as $K^2 = 0$ in the ambiguous region using an information-propagation scheme. Comparing our model with the model proposed by Ishikawa, although there is no difference aspect to completed depth, our model as the expression is extremely simple and implementable as a neural network using existing neurons. Our model described by Eq. (11) is mathematically equivalent to the model proposed by Satoh and Usui. We expect that Eq. (11) is a general formula for completion of visual information.

Moreover, two solutions (concave and convex surfaces) were obtained using the model. The solutions depend on the initial values necessary for numerical simulation of the steepest descent method.

A new characteristic of depth perception was revealed in completion of the ambiguous region. Completed surfaces on the ambiguous region depend on the ISI duration and the shape of prior stimuli. Short ISIs show a positive correlation of perception between the prior and post stimuli, but longer ISIs show an opposite phenomenon. We present a mathematical model to account for the unforeseen phenomena. However, we have not reproduced temporal perceptual alternation using our model because we expect to introduce adaptation effects and the dynamics of Z among ISI for original energy function without using $\phi(x, y)$.

Future works include reproduction of perceptual alternation in a certain ISI using our model and investigation of the physiological evidence supporting our model.

7 Appendix

Appendix A

The update rule of decreasing $\iint_B K(x, y)^2 dx dy$ is derived using the steepest descent method as the following complex equation.

$$\begin{aligned} \frac{\partial Z(x, y, t)}{\partial t} = & (-4Z_{yy} Z_{xy}^4 + 36Z_y^2 Z_{yy} Z_{xy}^4 - 4Z_{yy} Z_x^2 Z_{xy}^4 + 80Z_y Z_x Z_{xy}^5 - 32Z_y Z_{xy}^3 Z_{xyy} \\ & - 32Z_y^3 Z_{xy}^3 Z_{xyy} - 32Z_y Z_x^2 Z_{xy}^3 Z_{xyy} + 8Z_{yy}^2 Z_{xy}^2 Z_{xx} - 72Z_y^2 Z_{yy}^2 Z_{xy}^2 Z_{xx} \\ & + 16Z_y Z_{yyy} Z_{xy}^2 Z_{xx} + 16Z_y^3 Z_{yyy} Z_{xy}^2 Z_{xx} + 8Z_{yy}^2 Z_x^2 Z_{xy}^2 Z_{xx} + 16Z_y Z_{yyy} Z_x^2 Z_{xy}^2 Z_{xx} \\ & - 160Z_y Z_{yy} Z_x Z_{xy}^3 Z_{xx} - 4Z_{xy}^4 Z_{xx} - 4Z_y^4 Z_{xy}^4 Z_{xx} + 36Z_x^2 Z_{xy}^4 Z_{xx} \\ & + 32Z_y Z_{yy} Z_{xy} Z_{xyy} Z_{xx} + 32Z_y^3 Z_{yy} Z_{xy} Z_{xyy} Z_{xx} + 32Z_y Z_{yy} Z_x^2 Z_{xy} Z_{xyy} Z_{xx} \\ & + 16Z_x Z_{xy}^2 Z_{xyy} Z_{xx} + 16Z_y^2 Z_x Z_{xy}^2 Z_{xyy} Z_{xx} + 16Z_x^3 Z_{xy}^2 Z_{xyy} Z_{xx} - 2Z_{xyy}^2 Z_{xx} \\ & - 4Z_y^2 Z_{xyy}^2 Z_{xx} - 2Z_y^4 Z_{xyy}^2 Z_{xx} + \dots + \text{(100 terms)} + 2Z_{yy}^2 Z_x^2 Z_{xxxx} \\ & + 2Z_y^2 Z_{yy}^2 Z_x^2 Z_{xxxx} + Z_{yy}^2 Z_x^4 Z_{xxxx}) / (1 + Z_x^2 + Z_y^2)^6 \end{aligned}$$

Appendix B

We prove the proposition of Eq. (7). Here, K and $\bar{\kappa}, \bar{\mu}$ are rotation invariant. Therefore, we can calculate them on the local coordinate system (ξ, η) so that $I_\eta = 0$ (see Fig. 11a). First, we prove the case of $Z_x(x, y) \neq 0, Z_y(x, y) \neq 0$. Curvature is rotation invariant. Gaussian curvature can be formulated as shown below.

$$K(x, y) = \frac{Z_{\eta\eta}(x, y)Z_{\xi\xi}(x, y) - Z_{\eta\xi}^2(x, y)}{(1 + Z_\xi^2(x, y) + Z_\eta^2(x, y))^2} \quad (\text{B.1})$$

$\bar{\kappa}, \bar{\mu}$ is defined as follows using the local coordinate system (ξ, η) in this paper.

$$\bar{\kappa}(x, y) = \kappa(x, y)Z_\xi(x, y) = Z_{\eta\eta}(x, y) \quad (\text{B.2})$$

$$\bar{\mu}(x, y) = \mu(x, y)Z_\xi(x, y) = Z_{\eta\xi}(x, y) \quad (\text{B.3})$$

Consequently, if $\bar{\kappa}(x, y) = \bar{\mu}(x, y) = 0$, then $K(x, y) = 0$. If $Z_x(x, y) = Z_y(x, y) = 0$, then $Z_\xi(x, y) = 0$. It is readily apparent.

Appendix C

To describe the energy function proposed in Section 2 using $\phi(x, y)$, we give a proof of the following relation.

$$E_1[\phi] = 0 \implies E_{\text{flat}}[Z] = 0 \quad (\text{C.1})$$

First, the following propositions are clearly true.

$$E_1[\phi] = 0 \Leftrightarrow \forall (x, y) \in B; \|\nabla\phi(x, y)\|^2 = 0 \quad (\text{C.2})$$

$$\forall (x, y) \in B; \|\nabla\phi(x, y)\|^2 = 0 \Leftrightarrow \forall (x, y) \in B; \phi(x, y) = \text{const} \quad (\text{C.3})$$

1 Therefore, it suffices to show the following proposition.

$$\forall(x, y) \in B; \phi(x, y) = \text{const} \Rightarrow E_{\text{flat}}[Z] = 0 \quad (\text{C.4})$$

2 $\partial Z(x, y)/\partial \phi$ was described by

$$\frac{\partial Z}{\partial \phi} = \begin{cases} Z_{\wedge}(x, y) & \text{if } \phi > 0 \\ 0 & \text{if } \phi = 0. \\ Z_{\wedge}(x, y) & \text{otherwise} \end{cases} \quad (\text{C.5})$$

3 In the case of $\phi > 0$, $Z_x(x, y)$ is described by

$$4 \quad Z_x(x, y) = \frac{\partial Z}{\partial x} = \frac{\partial Z}{\partial \phi} \cdot \frac{\partial \phi}{\partial x} = Z_{\wedge}(x, y) \cdot \frac{\partial \phi}{\partial x}.$$

5 Now, because of $\phi(x, y) = \text{const}$, $\partial \phi(x, y)/\partial x = 0$. Then, $Z_x(x, y) = 0$.

6 Similarly, $Z_y(x, y) = 0$.

7 Then, $\bar{\kappa}(x, y) = \bar{\mu}(x, y) = 0$.

8 The case of $\phi < 0$ is proved similarly. In the case of $\phi = 0$, it is readily apparent.

9 Therefore, if $\phi(x, y) = \text{const}$, then

$$10 \quad E_{\text{flat}}[Z] = \iint_B (\bar{\kappa}^2 + \bar{\mu}^2) \, dx dy = 0.$$

11 Consequently,

$$12 \quad E_1[\phi] = 0 \Rightarrow E_{\text{flat}}[Z] = 0$$

13 Acknowledgments

14 Mr. Tetsumasa Asano is acknowledged for his helpful comments and suggestions. This
15 work was partially supported by JSPS KAKENHI Grant Nos. 24500371 and 16K00204.

16

17 References

18 Belhumeur, P. N. (1996). A Bayesian Approach to Binocular Stereopsis. *International*

19 *Journal of Computer Vision*, 19(3), 237–260. <http://doi.org/10.1007/BF00055146>

20 Belhumeur, P. N., & Mumford, D. (1992). A Bayesian treatment of the stereo

21 correspondence problem using half-occluded regions. *Proceedings 1992 IEEE Computer*
22 *Society Conference on Computer Vision and Pattern Recognition*, 506–512.

23 <http://doi.org/10.1109/CVPR.1992.223143>

24 Brainard, D. H. (1997). The Psychophysics Toolbox. *Spatial Vision*, 10(4), 433–436.

25 Georgeson, M. A., Yates, T. T. A., & Schofield, A. J. (2009). Depth propagation and surface
26 construction in 3-D vision. *Vision Research*, 49(1), 84–95.

27 <http://doi.org/10.1016/j.visres.2008.09.030>

28 Ishikawa, H. (2007). Total Absolute Gaussian Curvature for Stereo Prior. In Y. Yagi, S. B.

1 Kang, I. S. Kweon, & H. Zha (Eds.), *Computer Vision -- ACCV 2007: Eighth Asian*
2 *Conference on Computer Vision, Tokyo, Japan, November 18-22, 2007, Proceedings,*
3 *Part II* (pp. 537–548). Berlin, Heidelberg: Springer Berlin Heidelberg.
4 http://doi.org/10.1007/978-3-540-76390-1_53

5 Ishikawa, H., & Geiger, D. (2006). Illusory volumes in human stereo perception. *Vision*
6 *Research*, 46(1-2), 171–8. <http://doi.org/10.1016/j.visres.2005.06.028>

7 Katsuyama, N., Naganuma, T., Sakata, H., & Taira, M. (2006). Coding of 3D curvature in
8 the parietal cortex (area CIP) of macaque monkey. In K. Murase, K. Sekiyama, T.
9 Naniwa, N. Kubota, & Sitte, J. (Eds.), *Proceedings of the Third International*
10 *Symposium on Autonomous Minirobots for Research and Edutainment (AMiRE 2005)*
11 (pp. 1–7). Berlin, Heidelberg: Springer Berlin Heidelberg. [http://doi.org/10.1007/3-540-](http://doi.org/10.1007/3-540-29344-2_27)
12 [29344-2_27](http://doi.org/10.1007/3-540-29344-2_27)

13 Kleiner, M. D., & Brainard, D. P. (2007). What's new in Psychtoolbox-3? In *Perception 36*
14 *ECVP Abstract Supplement*.

15 Koenderink, J. J. (1990). *Solid shape. Artificial intelligence*.

16 Lindeberg, T. (1993). *Scale-space theory in computer vision*. USA: Kluwer Academic
17 Publishers.

18 Marr, D., & Poggio, T. (1976). Cooperative computation of stereo disparity. *Science*,
19 *194*(4262), 283–287. <http://doi.org/10.1126/science.968482>

20 Nishina, S., & Kawato, M. (2004). A computational model of spatio-temporal dynamics
21 depth filling-in. *Neural Networks: The Official Journal of the International Neural*
22 *Network Society*, 17(2), 159–63. <http://doi.org/10.1016/j.neunet.2003.09.004>

23 Pelli, D. G. (1997). The VideoToolbox software for visual psychophysics: transforming
24 numbers into movies. *Spatial Vision*. <http://doi.org/10.1163/156856897X00366>

25 Poggio, G. F., & Poggio, T. (1984). The Analysis of Stereopsis. *Annu. Rev. Neurosci.*, 7, 379–
26 412.

27 Pollard, S. B., Mayhew, J. E., & Frisby, J. P. (1985). PMF: a stereo correspondence
28 algorithm using a disparity gradient limit. *Perception*, 14(4), 449–70. Retrieved from
29 <http://www.ncbi.nlm.nih.gov/pubmed/3834387>

30 Satoh, S., & Usui, S. (2008). Computational theory and applications of a filling-in process at
31 the blind spot. *Neural Networks: The Official Journal of the International Neural*
32 *Network Society*, 21(9), 1261–71. <http://doi.org/10.1016/j.neunet.2008.05.001>

33 Würger, S. M., & Landy, M. S. (1989). Depth interpolation with sparse disparity cues.
34 *Perception*, 18(1), 39–54. <http://doi.org/10.1068/p180039>

35